

Er³⁺-Doped Lithium Niobate Thin Film: A Material Platform for Ultracompact, Highly Efficient Active Microphotonic Devices

Qing Xu, Feng Chen, Zhao-Xi Chen, Cheng Wang, Edwin Yue-Bun Pun, and De-Long Zhang*

Lithium niobate on insulator (LNOI) has already become a promising material platform for ultracompact, high-performance, and low-cost passive microphotonic devices. However, studies on an active LNOI platform are relatively slow. Current work aims at developing an important integrated photonic piece, an active LNOI thin film and waveguide. Herein, it is first demonstrated that a full wafer-scale (3 in. in diameter) Er³⁺-doped LNOI (Er:LNOI) wafer can be fabricated by directly ion-beam slicing a commercially bulk Er³⁺-doped lithium niobate wafer. Then, a number of rib-type waveguides with a cross-section $<1\ \mu\text{m}^2$ are patterned on its surface using mature nanostructuring technologies. Further optical and spectroscopic characterization results confirm the applicability of the Er:LNOI wafer to the fabrication of an active waveguide. The success in fabrication of Er³⁺-doped LNOI thin film and waveguides enables the establishment of an active LNOI platform and opens the possibility of developing ultracompact active microphotonic devices, which may find wide applications in the fields of optical communications, nonlinear optics, microwave photonics, and novel photonic systems such as parity-time symmetric systems.

1. Introduction


Si photonics is established on the basis of the silicon-on-insulator (SOI) waveguide. It is promising for high-density modern integrated optics and is currently an international hot research field.^[1–3] Similar waveguides can be realized on the basis of submicrometer thin films of lithium niobate (LiNbO₃) on insulator (LNOI).^[4–6] The waveguide based on LNOI combines the merits of the waveguide itself and the excellent electro-optic, acousto-optic, and nonlinear optical properties of LiNbO₃ (LN). The effective combination, together with the possibility of producing a high-quality waveguide of low loss ($<0.1\ \text{dB cm}^{-1}$ at $1.55\ \mu\text{m}^{[7]}$) using mature technologies, makes LNOI more promising. LNOI has already become an important platform for developing various ultracompact passive microphotonic devices. These devices are highly efficient, possess great application

prospect, and are expected to replace the conventional devices. Most previous works focused on the passive LNOI waveguides and related devices. To date, many ultracompact passive microphotonic LNOI devices have been demonstrated. These include (complementary metal oxide semiconductor (CMOS)-compatible) electro-optic modulators,^[8–11] microdisks, and microring resonators,^[4,12–16] grating couplers,^[17] transverse-electric (TE)/transverse-magnetic (TM)-pass polarizers,^[18] quantum photonic devices,^[19,20] metasurfaces,^[21] and various nonlinear optical devices based on periodically poled LNOI waveguides.^[22,23]

Active waveguides and devices are also important optical components in the building blocks of an integrated optical platform. Obviously, it is more attractive and promising to develop the active devices based on an SOI waveguide. Over the past years, people have put a lot of effort into the development of active devices based on SOI waveguides.^[24–27] It has been seldom successful because of two intrinsic problems. On one hand, significant background absorption of the silicon material itself results in large waveguide loss and low pumping efficiency. On the other hand, the active ions in a Si substrate display poorer spectroscopic property (the Er³⁺ absorption cross-section in a Si substrate is four times smaller than that in a LiNbO₃ crystal).^[26–29] It is imperative to explore other feasible ways to obtain highly efficient ultracompact microphotonic

Q. Xu, F. Chen, D.-L. Zhang
Department of Opto-electronics and Information Engineering
School of Precision Instruments and Opto-electronics Engineering
Key Laboratory of Optoelectronic Information Science & Technology
(Ministry of Education)
Tianjin University
Tianjin 300072, China
E-mail: dlzhang@tju.edu.cn

Z.-X. Chen, C. Wang, E. Y.-B. Pun
Department of Electrical Engineering & State Key Laboratory of Terahertz
and Millimeter Waves
City University of Hong Kong
Kowloon, Hong Kong, China

 The ORCID identification number(s) for the author(s) of this article can be found under <https://doi.org/10.1002/adpr.202100081>.

© 2021 The Authors. Advanced Photonics Research published by Wiley-VCH GmbH. This is an open access article under the terms of the Creative Commons Attribution License, which permits use, distribution and reproduction in any medium, provided the original work is properly cited.

DOI: 10.1002/adpr.202100081

active devices. One possible way to solve the problems that the rare-earth-doped SOI active waveguides suffer from is to replace the rare-earth-doped SOI active waveguide with a rare-earth-doped LNOI waveguide. As stated earlier, the LNOI waveguide effectively combines the merits of the waveguide with the excellent properties of the LiNbO₃ crystal itself. Moreover, rare-earth ions can be easily doped into the LiNbO₃ substrate to get an active material. In addition, the Er³⁺ ion in LiNbO₃ displays excellent spectroscopic properties. These merits of the rare-earth-doped LiNbO₃ crystal have already led to demonstration of a whole family of efficient Ti:Er:LiNbO₃ waveguide lasers (amplifiers) and nonlinear optical devices based on periodically poled LiNbO₃ waveguides.^[30–39] It is no doubt that these merits would also enable us to develop highly efficient active microphotonic devices based on rare-earth-doped LNOI. Recently, on-chip erbium-doped LNOI lasers and amplifiers have been successfully demonstrated,^[40–48] and these devices show that the rare-earth-doped LNOI has great potential for efficient laser sources and broadband amplification. In comparison, less work has been done on the material properties of the rare-earth-doped LNOI thin film itself, which are basic knowledge for the design and fabrication of an efficient active device. This article focuses on this aspect of study, and reports here the fabrication and characterization results of an Er:LNOI thin film and active waveguide. Characterizations were performed on the refractive index, Er³⁺ spectroscopic properties, and crystalline phase of the Er:LNOI thin film, as well as on waveguiding and amplification properties of the Er:LNOI active waveguide.

2. Fabrication of Er:LNOI Thin Film and Waveguides

Over the past years, the authors have expended a great deal of effort on exploring a feasible technology to fabricate a rare-earth-doped LNOI thin film and therefore establish a technical supporting platform for the development of various highly efficient ultracompact microphotonic active devices. A few methods have been attempted. We first attempted the conventional smart-cut method, that is, crystal ion slicing an Er³⁺-doped LiNbO₃ substrate prepared by thermal diffusion of a homogeneously coated Er metal thin film. The result shows that it is not a reliable method because the very long Er³⁺ diffusion procedure (over 100 h at 1130 °C) either increases the roughness or causes slight deformation of the diffused surface. We also attempted the method of mechanically grinding the rear surface of the Er³⁺-diffusion-doped LiNbO₃ substrate. However, cracking usually takes place for the substrate as its thickness is reduced to several tens of microns. So, this is also not a feasible method to obtain an erbium-doped thin film with submicrometer thickness. Recently, we further attempted the method of ion slicing a homogeneously Er³⁺-doped LiNbO₃ substrate grown by traditional Czochralski technique. The result shows that the method is feasible and has higher reliability. Based on the prepared Er:LNOI thin film, we have successfully fabricated some active waveguides.

A 0.5 mol% Er³⁺-doped LiNbO₃ single-crystal plate (3 in. in diameter and 0.5 mm in thickness), which was cut from a boule grown at a congruent point by traditional Czochralski technique, was used for fabrication of the Er:LNOI thin film after optical

polish to its two surfaces. A detailed procedure for the fabrication of the Er:LNOI thin film is described subsequently. It is based on the traditional smart-cut or crystal ion-slicing method, which consists of two steps: crystal ion slicing based on He⁺ implantation and subsequent wafer bonding. The smart-cut process was performed with the services of NANOLN (Jinan Jingzheng Electronics Co., Ltd.). The full wafer fabrication process is schematically sketched in **Figure 1**.

First of all, crystal ion slicing was done for the homogeneously Er³⁺-doped LiNbO₃ (Er:LN) single-crystal wafer plate to get the Er:LN thin film. To achieve that, the homogeneously Er³⁺-doped LiNbO₃ wafer (Z-cut) 3 in. in diameter (substrate A) was implanted by He⁺ ions (200 keV) with a higher dose of 4×10^{16} ions cm⁻². After the implantation, an amorphous layer was formed underneath the crystal surface, and defined a “cleavage plane” within the crystal. Another Z-cut LiNbO₃ handle sample (substrate B) was first coated with a 1.3 μm thick SiO₂ layer by plasma-enhanced chemical vapor deposition and then annealed at 450 °C for 8 h to drive off the gases trapped in the oxide layer. After chemical mechanical polishing (CMP), the surface roughness was reduced to 0.5 nm, which enabled direct wafer bonding. The bonded pair of samples was then annealed at 165 °C for 16 h and 190 °C for 6 h to increase the bonding strength. After an additional anneal at 230 °C for 2 h, the sample split along the He⁺ implanted layer, that is, along the cleavage plane. As a result, a thin film of Er:LN was sliced from the Er³⁺-doped LiNbO₃ single-crystal plate by the He⁺ ions. Afterward, it was annealed at 450 °C for 8 h to minimize ion-implantation-induced material damage (amorphization) and hence recover the electro-optic and nonlinear optical properties, as well as significantly reduce the surface roughness. Finally, CMP was performed on the Er:LNOI to degrade the surface roughness (<0.5 nm).

The Er:LNOI wafer was cut into some pieces with a size of 10 mm × 10 mm. We selected one piece and fabricated some rib-type waveguides on its surface. **Figure 2** shows the flow process of the fabrication. The waveguides were fabricated with a technological process in a sequence of the following four steps. 1) NiCr mask deposition: a number of 0.6–2.0 μm-wide, 250 nm

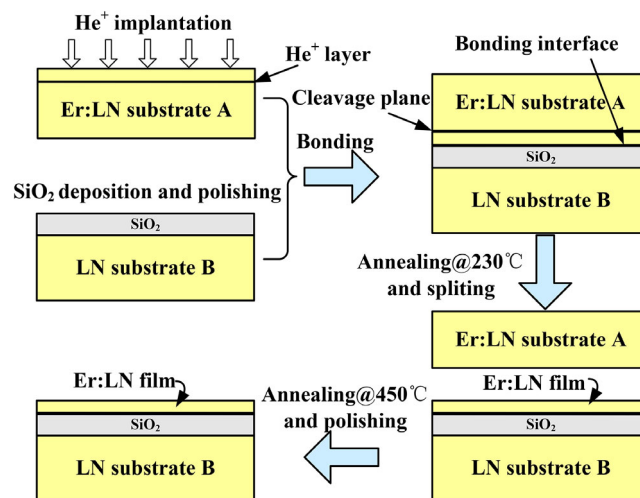


Figure 1. Flow-process diagram for fabrication of 3 in. Er³⁺-doped LNOI wafer by crystal ion slicing and wafer bonding.

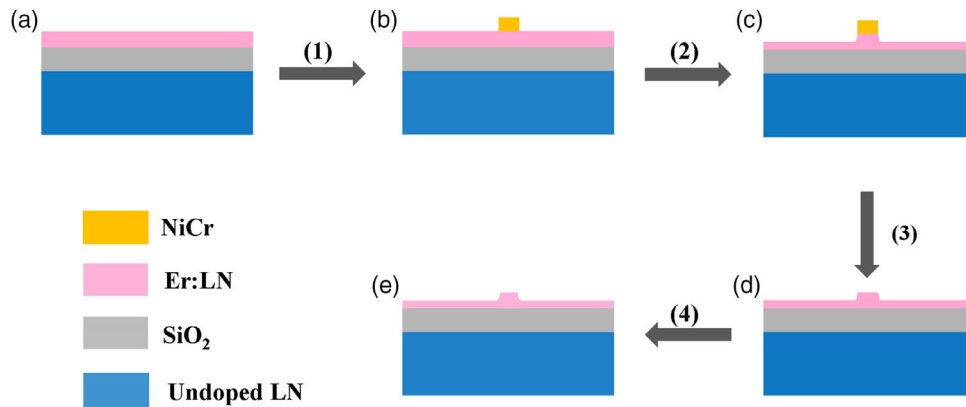


Figure 2. Flow-process diagram for fabrication of Er:LNOI active waveguides by EBL, RIE, and CMP techniques.

thick NiCr strips were delineated onto the top surface of the Er:LNOI thin film successively by electron beam lithography (EBL), physical vapor deposition (PVD), and lift-off processes. 2) Reactive ion etching (RIE): the Er:LNOI thin-film part without the NiCr mask cover was etched using a dry RIE technique. As a result, some rib-type waveguides were fabricated. 3) NiCr removal: the NiCr mask was removed. 4) CMP: CMP was finally performed on the surfaces and sidewalls of the Er:LNOI waveguides to degrade the roughness there.

After the fabrication, the optical and spectroscopic characteristics of both the Er:LNOI thin film and the waveguides were fully characterized.

3. Results and Discussion

3.1. Er:LNOI Thin Film

Figure 3a shows a photograph of the 0.5 mol% Er³⁺-doped Z-cut LNOI wafer (3 in. in diameter) prepared by the smart-cut method. The surface roughness was measured by an atomic force microscope. It has a root mean square (rms) value <0.5 nm. **Figure 3b,c** shows the Er:LNOI pieces cut from the wafer. Their thicknesses were measured by a white-light interferometer (with an accuracy <1 nm). The results are displayed in **Figure 4**. One can see that the thickness of the 3 in. Er³⁺-doped Z-cut LNOI wafer fabricated varies within 670–720 nm.

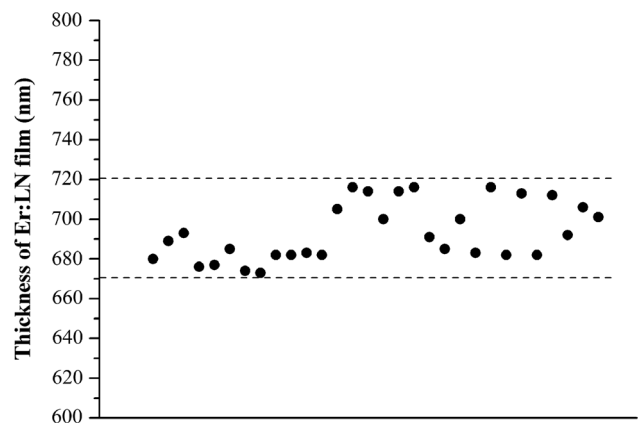


Figure 4. Thickness of Er:LNOI pieces cut from 3 in. Er³⁺-doped Z-cut LNOI wafer.

The prepared Er:LNOI piece sample was optically characterized. As we know, the LNOI itself forms an air/LN/SiO₂ three-layer slab waveguide with a submicrometer thickness and a higher refractive index contrast. Of course, this is also the case for the Er:LNOI. The effective refractive indices of the TE and TM modes guided in the air/Er:LN/SiO₂ three-layer slab waveguide were measured at the wavelength 632.8 nm using a commercial Metricon 2010 prism coupler. **Figure 5** shows the

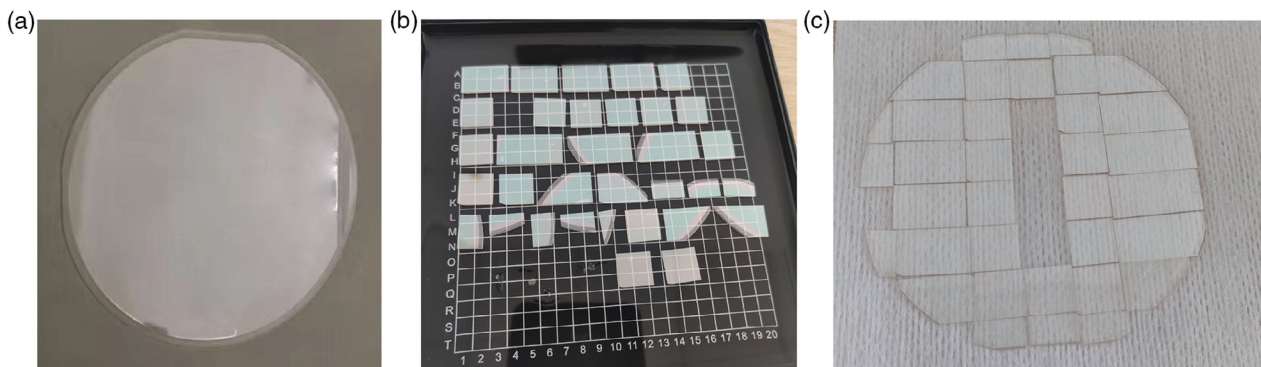


Figure 3. Photographs of a) 0.5 mol% Er³⁺-doped Z-cut LNOI wafer (3 in. in diameter), b,c) Er:LNOI pieces after cutting.

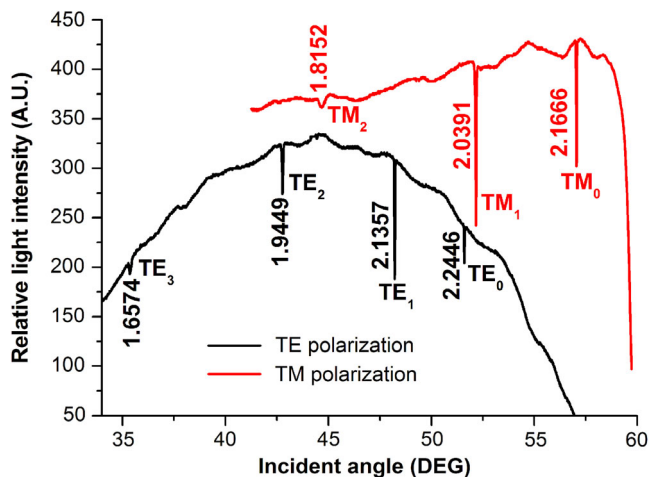


Figure 5. Patterns of relative intensity of TE- and TM-polarized 632.8 nm light as a function of incident angle inside prism.

patterns of relative intensity of TE- and TM-polarized 632.8 nm light reflected from the Er:LNOI slab waveguide surface. The light intensity was measured as a function of the incident angle inside the prism. The guided modes are assigned and indicated on each pattern. The data indicated on each dip of the patterns are the effective index value of the corresponding mode guided. With known effective index values of three or more modes, the refractive index profile of a thin film can be constructed using the inverse Wentzel–Kramers–Brillouin (IWKB) method. The more the number of the modes is, the more accurate the index profile constructed is. In respect to the air/Er:LN/SiO₂ three-layer slab waveguide concerned here, as shown in Figure 5, under the TE polarization, under which the guided modes involve n_o for a Z-cut substrate, four modes, named TE₀, TE₁, TE₂, and TE₃ with a mode index of 2.2446, 2.1357, 1.9449, and 1.6574, respectively, can be resolved. Under the TM polarization, under which the guided modes involve both n_e and n_o , only three modes, named TM₀, TM₁, and TM₂, with a mode index of 2.1666, 2.0391, and 1.8152, respectively, could be resolved. Fewer modes result in larger error of the index profile constructed using the IWKB method. To obtain more accurate material index data, we used the Marcatili’s approximation method to analyze the air/Er:LN/SiO₂ three-layer slab waveguide studied here, in which the Er:LN layer is assumed to have a step-index profile. The analyzed results are brought together in Table 1 in comparison with the data of the Er³⁺-doped bulk LN crystal plate with a thickness of 0.5 mm. The analysis shows that the Er:LN thin film has a refractive index of $n_o = 2.2801$ and $n_e = 2.2080$, which are considerably different from the corresponding value of the Er³⁺-doped bulk

Table 1. Refractive index values of Er³⁺-doped bulk LN and Er:LNOI thin film before and after heat treatment at 500 °C for 10 h.

Material	n_o	n_e
Er:LNOI thin film	2.2801	2.2080
Er ³⁺ -doped bulk LN (0.5 mm thick)	2.2862	2.2026
Er:LNOI thin film annealed at 500 °C/10 h	2.2862	2.2026

LN: $n_o = 2.2862$ and $n_e = 2.2026$. Their difference, ≈ 0.006 in case of both n_o and n_e , considerably exceeds the measurement error of 0.001. It is associated with ion-implantation-induced lattice damage, which results in a slight decrease of n_o whereas there is a slight increase of n_e as shown previously. A postannealing treatment at 500 °C for 10 h makes the lattice and therefore the refractive indices completely recover, as shown in Table 1.

The analysis based on the Marcatili’s approximate method also gives the thickness information of the Er:LN layer. The TE mode analysis gives a thickness value of 683 nm and the TM mode analysis gives 684 nm, which are consistent with the results given in Figure 4.

With respect to the fabrication of the Er:LNOI thin film, there are a few points to be stressed. 1) It is essential to give a short explanation for the ion-slicing principle. In the implanted layer, the helium ions form gaseous bubbles during the annealing process. This phenomenon is referred to as “blistering.” The thermally induced helium blisters give rise to exfoliation of the He⁺-implanted layer from the Er:LN plate. In other words, the heating causes expansion of helium blisters in the implanted layer, local cracks, and final exfoliation of the Er:LN layer. Because the heat treatment needs >220 °C for the split-off of the Er:LN plate, the two materials bonded may have different thermal expansion effects, resulting in a mismatch of thermal expansion and therefore formation of a mechanical stress, which may induce cracking of the Er:LN thin film. The problem can be solved using the bonding technique. 2) The thickness of the sliced film is determined by the implantation depth of He⁺ ions, and the implantation energy determines the depth position of the cleavage plane. The required film thickness for a particular application can be thus controlled by the implantation energy. The empirical relation is given by $H \approx 3E + 70$ (nm), in which H denotes the Er:LN thin film thickness in nanometers and E represents the He⁺ implantation energy in kiloelectronvolts. 3) As mentioned earlier, high-temperature anneal may help to minimize the material damage induced by ion implantation, recover electro-optic and nonlinear properties, and significantly reduce the surface roughness. However, the working temperature of the Er:LNOI thin film cannot exceed 550 °C; otherwise, there is an adhesion problem between SiO₂ and LN. To promote the annealing temperature, one should seek other insulating materials, by which the interface bonded can stand an anneal at a higher temperature, to replace the SiO₂.

3.2. Er:LNOI Active Waveguide

To verify the applicability of the Er:LNOI thin film prepared, we selected a piece of Er:LNOI thin film, fabricated a number of 0.6–2.0 μm wide rib-type waveguides on its surface, and did the optical and spectroscopic characterizations.

The morphology feature of the fabricated Er:LNOI rib-type waveguides was characterized first. Figure 6a shows the top view of the waveguides fabricated on the surface of the Z-cut Er:LNOI thin film. The separation of two adjacent waveguides is 50 μm. Figure 6b shows a cross-section of a rib-type waveguide with a rib width of 745 nm and a rib height of 167 nm.

The waveguide characteristics of the Er:LNOI waveguides were studied experimentally. The end-fire coupling technique

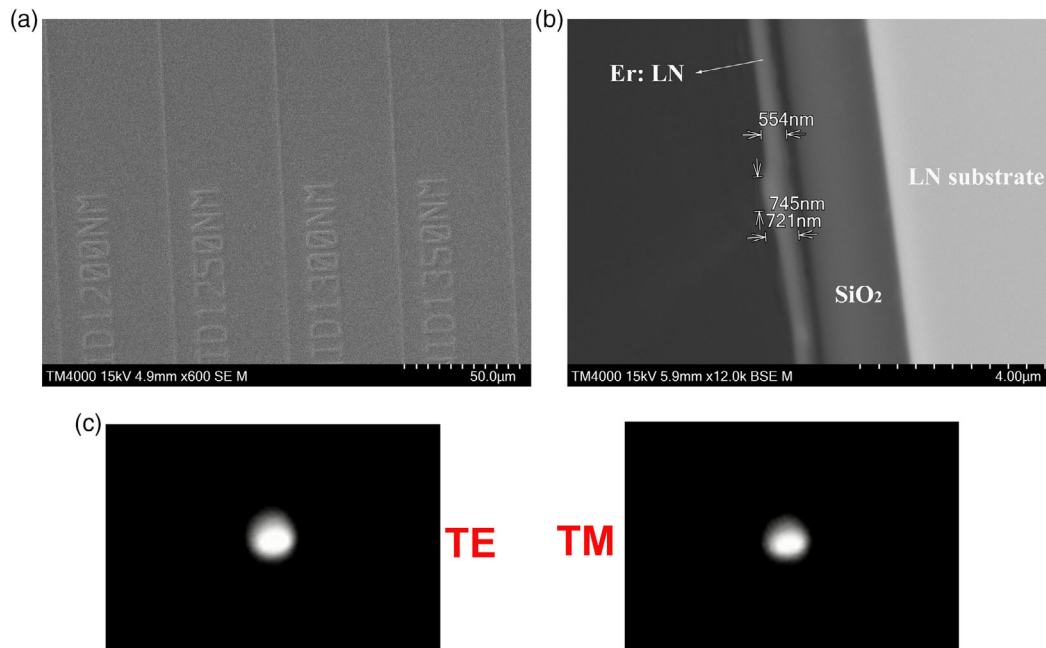


Figure 6. SEM images of a) top view and b) cross-section of the waveguide(s) fabricated on the surface of the Z-cut Er:LNOI thin film. c) TE and TM near-field mode patterns at 1.5 μm wavelength.

was used to observe and capture the near-field pattern of the guided mode. The experiment was conducted by launching into a waveguide a TE- or TM-polarized 1.5 μm light via endface butt coupling between a lensed fiber and the waveguide. The magnified near-field image of the guided mode was projected onto an infrared camera through a 20 \times microscope objective with a numerical aperture of 0.4. Figure 6c shows the TE and TM near-field mode patterns of the Er:LNOI waveguide with a rib width of 1.5 μm . It supports single-mode propagation of either a TE or a TM mode at the 1.5 μm wavelength.

Figure 7 shows the TE- and TM-mode light intensity distributions (blue balls) along the width x and depth y directions. The light intensity of the guided mode follows a square of cosine function in both the x and y directions, consistent with waveguide theory. The red lines represent the best fits by a square of a cosine function. At $1/e^2$ light intensity, the TE mode size is $W_x \times W_y = 0.96 \times 0.33 \mu\text{m}^2$ and the TM mode size is $W_x \times W_y = 0.8 \times 0.35 \mu\text{m}^2$. We note that both have similar smaller values of $\approx 0.3 \mu\text{m}^2$, showing that ultracompact confinement to either the TE or the TM single mode could be realized in the active Er:LNOI waveguide.

The waveguide loss is roughly evaluated from the insertion loss measured at the 1.31 μm wavelength, where Er^{3+} ground state absorption is absent. Measurements show that the insertion loss of the 1.5 μm wide, 4.8 mm long Er:LNOI waveguide is 15.0 and 19.0 dB for the TE and TM mode, respectively. The coupling loss is determined from the mismatch of mode fields and mechanical uncertainty. It is conservatively evaluated as 5.5 ± 1.0 dB for either the TE or TM mode at each side of the waveguide. From the values of the refractive index measured at the 1.31 μm wavelength, the loss due to the Fresnel reflection at the two interfaces of fiber–air and Er:LNOI–air is evaluated as

0.67 dB at the Er:LNOI–air interface and ≈ 0.15 dB at the fiber–air interface. The waveguide loss is then evaluated as 5.0 ± 4.0 and 13.0 ± 4.0 dB cm^{-1} for the TE and TM modes, respectively.

The waveguide loss was also evaluated at the 1531.6 nm wavelength, at which the measured insertion loss is 22/26 dB for the TE/TM mode and the Er^{3+} absorption loss is similar to 7.4/5.4 dB for the TE/TM mode, evaluated from the Er^{3+} concentration and Er^{3+} absorption cross-section values. The coupling loss is similar to 5.5 ± 1.0 dB for either the TE or the TM mode. The waveguide loss is evaluated as 4.1 ± 4.0 and 16.4 ± 4.0 dB cm^{-1} for the TE and TM modes, respectively, which are similar to those figures evaluated at 1.31 μm . The large loss figures originate from large uncertainty of coupling loss caused by mechanical components (multiaxis stages) of our en-face coupling system.

Figure 8 shows the Er^{3+} green upconversion fluorescence spectrum ($^4S_{3/2} \rightarrow ^4I_{15/2}$ and $^2H_{11/2} \rightarrow ^4I_{15/2}$ electronic transitions) of the Er:LNOI waveguide under excitation of 980 nm wavelength (red plot). The inset shows strong green upconversion fluorescence emitted from one waveguide (see the bright line in the central part) under the 980 nm excitation, which indicates that the erbium ions inside the waveguide are well activated. For comparison, the spectrum of the Er:LN bulk material (blue plot) is also shown. One can see that the spectrum of the waveguide is similar to that of the bulk material (the slight relative intensity change from the waveguide to the bulk material is associated with that the Er^{3+} reabsorption, named also “radiation trapping,” which is more serious in the bulk material). **Figure 9** shows the amplified spontaneous emission (ASE) spectrum of 1.5 μm ($^4I_{13/2} \rightarrow ^4I_{15/2}$) electronic transition of Er^{3+} in the Er:LNOI waveguide, which was pumped at either the 980 nm wavelength (blue curve, $^4I_{15/2} \rightarrow ^4I_{11/2}$ electronic transition of Er^{3+}) or the 1480 nm

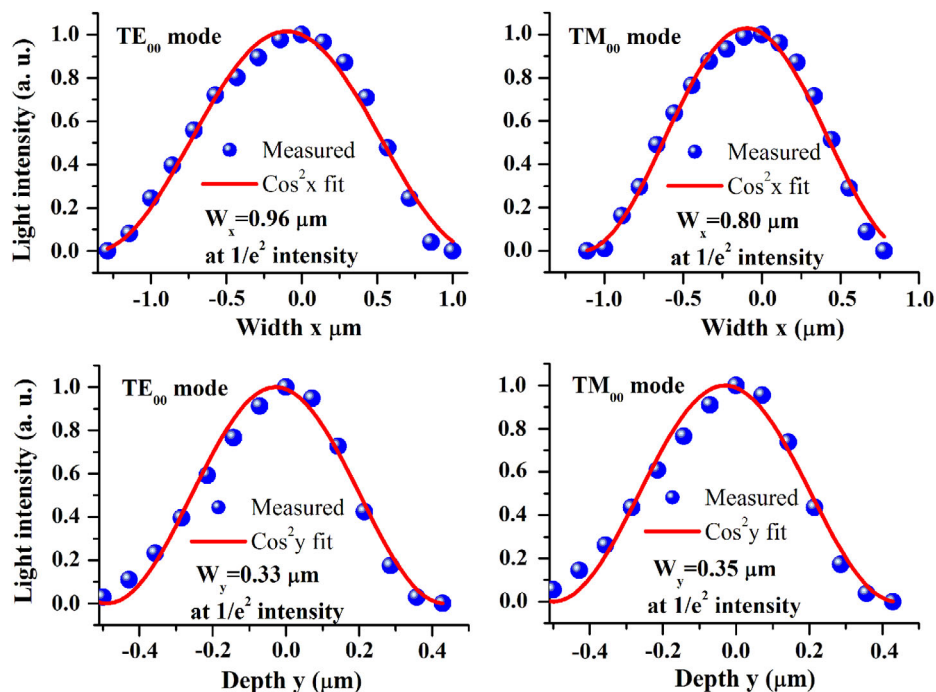


Figure 7. TE- and TM-mode light intensity distributions along a) width x and b) depth y directions of $1.5\ \mu\text{m}$ rib-wide Er:LNOI waveguide.

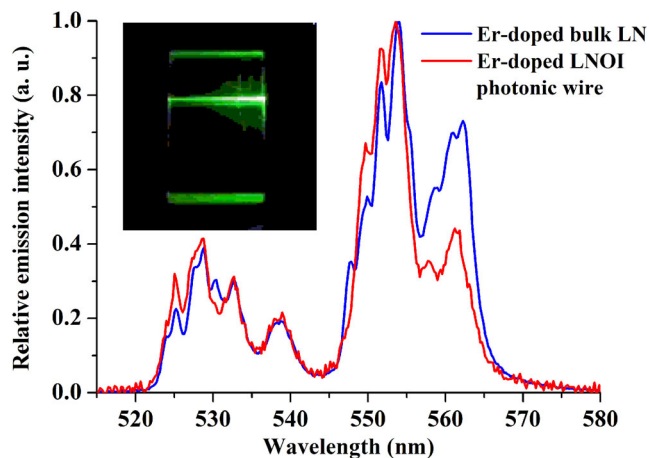


Figure 8. Er^{3+} green upconversion emission spectrum (520–580 nm) of the Er:LNOI waveguide under excitation of 980 nm wavelength (red plot). For comparison, the spectrum of the Er:LN bulk material (blue plot) is also shown. The inset shows the strong green upconversion fluorescence emitted from one waveguide (bright line in the central part) under excitation of 980 nm wavelength.

wavelength (red curve, ${}^4I_{15/2} \rightarrow {}^4I_{13/2}$ electronic transition of Er^{3+}). Emission peaks are indicated. As expected, the pump wavelength does not affect the spectral shape.

Because ASE is actually the amplified fluorescence of Er^{3+} in the waveguide, a comparison of the spectral feature of ASE with that of the fluorescence of the bulk Er:LN crystal may help us to determine the waveguide's crystalline phase. Comparison shows that the ASE spectrum of the Er:LNOI waveguide is similar to the fluorescence spectrum of the bulk Er:LN crystal, implying that

the Er^{3+} spectroscopic features in the waveguide are the typical spectroscopic features of Er^{3+} in the LN crystal, the Er^{3+} presence in the waveguide is in the form of the LN crystalline phase, and the He^+ -implantation-induced lattice damage is little.

Following the confirmation of the Er^{3+} spectroscopic features and crystalline phase, we further characterized the amplification performance of a $1.53\ \mu\text{m}$ small signal in the Er:LNOI active waveguide pumped at either 980 or 1480 nm wavelength. Figure 10 shows the experimental system used for the signal amplification measurement. A $1531.6\ \text{nm}$ small signal ($\approx 180\ \text{nW}$) following an attenuation is combined with a 980 or 1480 nm pump light by aid of a 980/1550 or a 1480/1550 nm WDM. The combined signal and pump light was butt coupled into the 4.8 mm long Er:LNOI waveguide with a rib height/width of $167\ \text{nm}/1.5\ \mu\text{m}$. To promote the coupling efficiency, a lensed fiber was used. The fiber-to-chip coupling loss was about 5.5 dB per facet at the 1531 nm wavelength. The polarization states of the signal and pump light were not resolved. The amplified signal and ASE outputs were butt coupled into a multimode fiber and measured by an optical spectrum analyzer (OSA). The signal enhancement (in unit of decibels), defined as the ratio of the signal out power when the pumping is on to that when the pumping is off, was measured as a function of the coupled pump power (at the input endface of the waveguide). Figure 11 shows the coupled pump power dependence of the signal enhancement factor of the 4.8 mm long Er:LNOI waveguide pumped at a) 980 nm and b) 1480 nm. In the case of the 980 nm pumping, we can see from Figure 11a that in the initial stage the signal enhancement factor increases with a rise in the 980 nm pump power. However, as the input pump power is higher than just 0.3 mW, the signal enhancement factor

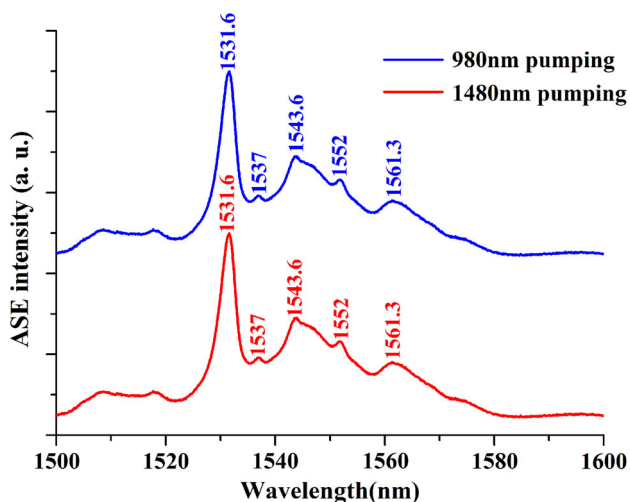


Figure 9. The ASE spectrum of the Er:LNOI waveguide pumped at a wavelength of 1480 nm (red) and 980 nm (blue).

drops abruptly due to the photorefractive effect at the 980 nm wavelength. The quite low pump power threshold of the photorefractive effect is associated with significantly increased light intensity in the Er:LNOI waveguide in comparison with a conventional Ti-diffused LN waveguide.

As the photorefractive effect is relatively weak in the 1.5 μm wavelength region, in the case of 1480 nm pumping, the signal enhancement factor increases stably with the increase of pump power. A saturation phenomenon takes place for a coupled 1480 nm pump power above only 3 mW, as shown in Figure 11b. The quite low saturation pump power is also correlated with the significantly increased light intensity in the waveguide structure. We further note that in the saturation region a signal enhancement factor of 5.4 dB cm^{-1} can be realized at quite a low pump level, 3 mW only. The measured signal enhancement in the Er:LNOI waveguide results from the pump-induced Er^{3+} population inversion indeed.

The signal enhancement obtained in this work is relatively low. To promote the signal enhancement, the following four measures

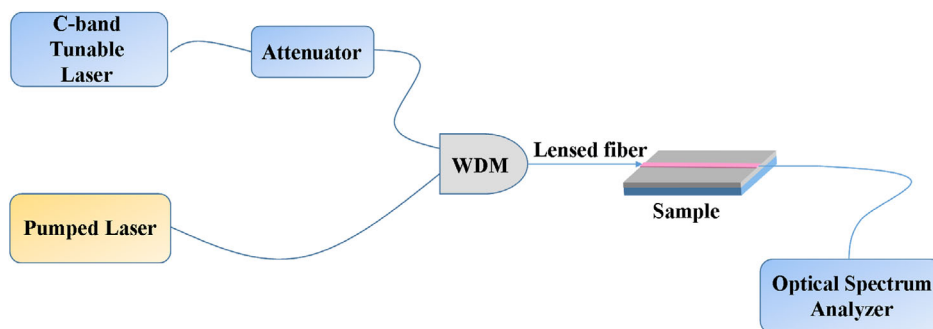


Figure 10. Experimental system for 1.53 μm small-signal-amplification characterization of Er:LNOI active waveguide pumped at either 980 or 1480 nm wavelength.

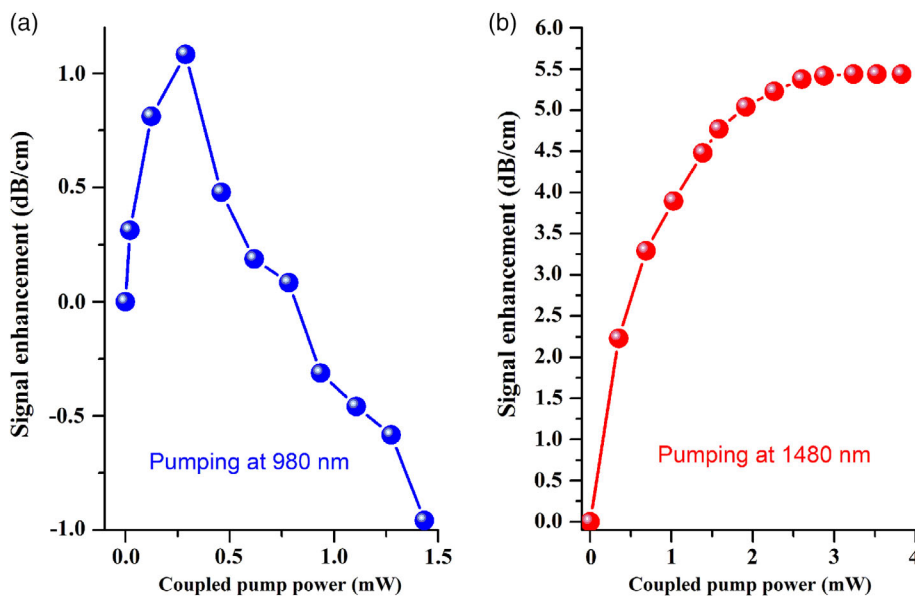


Figure 11. Signal enhancement factor of Er:LNOI waveguide as a function of input a) 980 nm and b) 1480 nm pump power.

should be taken in future works: 1) increasing the Er^{3+} concentration in the LNOI thin film, 2) increasing the length of the waveguide, 3) degrading the waveguide loss by optimizing the fabrication technology of the waveguide, and 4) degrading the coupling loss by designing and fabricating two appropriate waveguide couplers at the two sides of the waveguide. Another issue to be solved in the future is the photorefractive damage. The solution is to use a photorefractive-damage-resistant Er:LNOI thin film prepared by ion slicing a near-stoichiometric Er:LN crystal codoped with Mg^{2+} or Zr^{4+} so that a photorefractive-damage-resistant active Er:LNOI waveguide can be fabricated.

4. Conclusion

We have demonstrated successful preparation of a full wafer-scale (3 in. in diameter) Er:LNOI thin film by directly ion slicing a commercially bulk Er^{3+} -doped lithium niobate wafer. Applicability of the thin film is demonstrated by patterning a number of rib-type waveguides on its surface using mature nanostructuring technologies. We show that a saturation signal enhancement factor of 5.4 dB cm^{-1} is realized for a coupled 1480 nm pump power of only 3 mW. The measured signal enhancement in the waveguide indicates that the Er^{3+} ions inside the waveguide are well activated and the signal enhancement results from pump-induced Er^{3+} population inversion indeed, and therefore confirms the applicability of the Er:LNOI thin film to fabrication of an Er:LNOI active waveguide. The success in fabrication of the Er^{3+} -doped LNOI thin film and active waveguide opens the possibility of developing ultra-compact, highly efficient, and low-cost active microphotonic devices, which may find wide applications in loss-sensitive areas of optical communications, nonlinear optics, and microwave photonics. The added amplification functionality could also provide new functional degrees of freedom that enable new photonic systems such as parity-time symmetric systems.

This work provides comprehensive study of an important building block, active LNOI thin films and waveguides, of the LNOI photonic platform, and enables us to establish an active LNOI material platform for high-density photonic integrated circuits. Future works aim at improving and perfecting the platform through optimizations of materials, geometry, and fabrication technology of the waveguide.

Acknowledgements

Q.X and F.C. contributed equally to this study. This work was supported by the National Natural Science Foundation of China, under Project no. 61875148, and the Research Grants Council of the Hong Kong Special Administrative Region, China, under Project no. CityU 11210317.

Conflict of Interest

The authors declare no conflict of interest.

Data Availability Statement

Research data are not shared.

Keywords

active waveguides, Er^{3+} -doped lithium niobate on insulator, thin films

Received: March 17, 2021

Revised: July 14, 2021

Published online:

- [1] G. T. Reed, *Nature* **2004**, *427*, 595.
- [2] B. S. Song, S. Noda, T. Asano, Y. Akahane, *Nat. Mater.* **2005**, *4*, 207.
- [3] G. T. Reed, G. Mashanovich, F. Y. Gardes, D. J. Thomson, *Nat. Photonics* **2010**, *4*, 518.
- [4] M. Zhang, C. Wang, R. Cheng, A. Shams-Ansari, M. Loncar, *Optica* **2017**, *4*, 1536.
- [5] W. Sohler, R. M. De La Rue, *Laser Photonics Rev.* **2012**, *6*, A21.
- [6] G. Poberaj, H. Hu, W. Sohler, P. Guenter, *Laser Photonics Rev.* **2012**, *6*, 488.
- [7] A. Boes, B. Corcoran, L. Chang, J. Bowers, A. Mitchell, *Laser Photonics Rev.* **2018**, *12*, 1700256.
- [8] M. B. He, M. Y. Xu, Y. X. Ren, J. Jian, Z. L. Ruan, Y. S. Xu, S. Q. Gao, S. H. Sun, X. Q. Wen, L. D. Zhou, L. Liu, C. J. Guo, H. Chen, S. Y. Yu, L. Liu, X. L. Cai, *Nat. Photonics* **2019**, *13*, 359.
- [9] C. Wang, M. Zhang, X. Chen, M. Bertrand, A. Shams-Ansari, S. Chandrasekhar, P. Winzer, M. Loncar, *Nature* **2018**, *562*, 101.
- [10] G. Guarino, *Nat. Photonics* **2007**, *1*, 407.
- [11] M. Y. Xu, M. B. He, H. G. Zhang, J. Jian, Y. Pan, X. Y. Liu, L. F. Chen, X. F. Meng, H. Chen, Z. H. Li, X. Xiao, S. H. Yu, S. Y. Yu, X. L. Cai, *Nat. Commun.* **2020**, *11*, 3911.
- [12] M. Zhang, B. Buscaino, C. Wang, A. Shams-Ansari, C. Reimer, R. R. Zhu, J. M. Kahn, M. Loncar, *Nature* **2019**, *568*, 373.
- [13] C. Wang, M. J. Burek, Z. Lin, H. A. Atikian, V. Venkataraman, I. Huang, P. Stark, M. Loncar, *Opt. Express* **2014**, *22*, 30924.
- [14] J. Wang, F. Bo, S. Wan, W. Li, F. Gao, J. Li, G. Zhang, J. Xu, *Opt. Express* **2015**, *23*, 23072.
- [15] R. Wu, J. Zhang, N. Yao, W. Fang, L. Qiao, Z. Chai, J. Lin, Y. Cheng, *Opt. Lett.* **2018**, *43*, 4116.
- [16] J. Lin, Y. Xu, Z. Fang, M. Wang, J. Song, N. Wang, L. Qiao, W. Fang, Y. Cheng, *Sci. Rep.* **2015**, *5*, 8072.
- [17] A. Kar, M. Bahadori, S. B. Gong, L. L. Goddard, *Opt. Express* **2019**, *27*, 15856.
- [18] E. Saitoh, Y. Kawaguchi, K. Saitoh, M. Koshiba, *IEEE Photonics J.* **2013**, *5*, 6600610.
- [19] S. Aghaeimeibodi, B. Desiatov, J. H. Kim, C. M. Lee, M. A. Buyukkaya, A. Karasahin, C. J. K. Richardson, R. P. Leavitt, M. Loncar, E. Waks, *Appl. Phys. Lett.* **2018**, *113*, 221102.
- [20] A. A. Sayem, R. S. Cheng, S. H. Wang, H. X. Tang, *Appl. Phys. Lett.* **2020**, *116*, 151102.
- [21] B. F. Gao, M. X. Ren, W. Wu, H. Hu, W. Cai, J. J. Xu, *Laser Photonics Rev.* **2019**, *13*, 1800312.
- [22] M. Jankowski, C. Langrock, B. Desiatov, A. Marandi, C. Wang, M. Zhang, C. R. Phillips, M. Loncar, M. M. Fejer, *Optica* **2020**, *7*, 40.
- [23] Z. Z. Hao, L. Zhang, W. B. Mao, A. Gao, X. M. Gao, F. Gao, F. Bo, G. Q. Zhang, J. J. Xu, *Photonics Res.* **2020**, *8*, 311.
- [24] H. S. Rong, A. S. Liu, R. Jones, O. Cohen, D. Hak, R. Nicolaescu, A. Fang, M. Paniccia, *Nature* **2005**, *433*, 292.
- [25] H. S. Rong, R. Jones, A. S. Liu, O. Cohen, D. Hak, A. Fang, M. Paniccia, *Nature* **2005**, *433*, 725.
- [26] M. A. Lourenco, R. M. Gwilliam, K. P. Homewood, *Appl. Phys. Lett.* **2007**, *91*, 141122.
- [27] B. A. Andreev, Z. F. Krasilnik, D. I. Kryzhkov, D. V. Shengurov, A. N. Yablonskiy, V. P. Kuznetsov, *J. Lumin.* **2012**, *132*, 3148.

- [28] N. N. Ha, K. Dohnalová, T. Gregorkiewicz, J. Valenta, *Phys. Rev. B* **2010**, *81*, 195206.
- [29] K. E. Kudryavtsev, D. I. Kryzhkov, L. V. Krasilnikova, D. V. Shengurov, V. B. Shmagin, B. A. Andreev, Z. F. Krasilnik, *JETP Lett.* **2015**, *100*, 807.
- [30] N. A. Sanford, *IEEE J. Quantum Electron.* **1997**, *33*, 1626.
- [31] I. Baumann, S. Bosso, R. Brinkmann, R. Corsini, M. Dinand, A. Greiner, K. Schäfer, J. Söchtig, W. Sohler, H. Suche, R. Wessel, *IEEE J. Sel. Top. Quantum Electron.* **1996**, *2*, 355.
- [32] W. Sohler, H. Suche, in *Erbium-Doped Lithium Niobate Waveguide Lasers, Integrated Optical Circuits and Components: Design and Application* (Eds: E.J. Murphy), Marcel Dekker, Inc., Basel, New York **1999**, pp.127–159.
- [33] Ch. Becker, T. Oesselke, J. Pandavenes, R. Ricken, K. Rochhausen, G. Schreiber, W. Sohler, H. Suche, R. Wessel, S. Balsamo, I. Montrosset, D. Sciancalepore, *IEEE J. Sel. Top. Quantum Electron.* **2000**, *6*, 101.
- [34] P. Becker, R. Brinkmann, M. Dinand, W. Sohler, H. Suche, *Appl. Phys. Lett.* **1992**, *61* 1257.
- [35] J. Amin, J. A. Aust, N. A. Sanford, *Appl. Phys. Lett.* **1996**, *69*, 3785.
- [36] C. H. Huang, L. McCaughan, *IEEE J. Sel. Top. Quantum Electron.* **1996**, *2*, 367.
- [37] E. Cantelar, G. A. Torchia, J. A. Sanz-Garcia, P. L. Pernas, G. Lifante, F. Cusso, *Appl. Phys. Lett.* **2003**, *83*, 2991.
- [38] B. K. Das, R. Ricken, V. Quiring, H. Suche, W. Sohler, *Opt. Lett.* **2004**, *29*, 165.
- [39] G. Schreiber, D. Hofmann, W. Grundkotter, Y. L. Lee, H. Suche, V. Quiring, R. Ricken, W. Sohler, *Proc. SPIE Int. Soc. Opt. Eng.* **2001**, *4277*, 144.
- [40] J. Zhou, Y. Liang, Z. Liu, W. Chu, H. Zhang, D. Yin, Z. Fang, R. Wu, J. Zhang, W. Chen, Z. Wang, Y. Zhou, M. Wang, Y. Cheng, *arXiv: 2101.00783*, **2021**.
- [41] Q. Luo, C. Yang, Z. Hao, R. Zhang, D. Zheng, F. Bo, Y. Kong, G. Zhang, J. Xu, *Chin. Opt. Lett.* **2021**, *19*, 060008.
- [42] X. Yan, Y. Liu, J. Wu, Y. Chen, X. Chen, *arXiv: 2105.00214*, **2021**.
- [43] Z. Chen, Q. Xu, K. Zhang, W. H. Wong, D. L. Zhang, E. Y. B. Pun, C. Wang, *Opt. Lett.* **2021**, *46*, 1161.
- [44] D. F. Yin, Y. Zhou, Z. Liu, Z. Wang, H. Zhang, Z. Fang, W. Chu, R. Wu, J. Zhang, W. Chen, M. Wang, Y. Cheng, *Opt. Lett.* **2021**, *46*, 2127.
- [45] Q. Luo, C. Yang, R. Zhang, Z. Hao, D. Zheng, H. Liu, X. Yu, F. Gao, F. Bo, Y. Kong, G. Zhang, J. Xu, *arXiv: 2103.09558*, **2021**.
- [46] Q. Luo, Z. Z. Hao, C. Yang, R. Zhang, D. H. Zheng, S. G. Liu, H. D. Liu, F. Bo, Y. F. Kong, G. Q. Zhang, J. J. Xu, *Sci. China Phys. Mech. Astron.* **2021**, *64* 234263.
- [47] Y. A. Liu, X. S. Yan, J. W. Wu, B. Zhu, Y. P. Chen, X. F. Chen, *Sci. China Phys. Mech. Astron.* **2021**, *64*, 234262.
- [48] Z. Wang, Z. Fang, Z. Liu, W. Chu, Y. Zhou, J. Zhang, R. Wu, M. Wang, T. Lu, Y. Cheng, *Opt. Lett.* **2021**, *46*, 380.